TU Delft

Delft University of Technology

Chessboard FPA in 130-nm SiGe BiCMOS for High-Resolution Passive Terahertz Imaging

Document Version
Final published version

Licence
CC BY

Citation (APA)
Hoogelander, M., Spirito, M., Sutbas, B., Carta, C., Llombart, N., & Alonso-delPino, M. (2026). Chessboard FPA in 130-nm SiGe BiCMOS for High-Resolution Passive Terahertz Imaging. *IEEE Journal of Microwaves*, *6*(2), 334-349.
https://doi.org/10.1109/JMW.2026.3660185

Important note
To cite this publication, please use the final published version (if applicable).
Please check the document version above.

Copyright
In case the licence states "Dutch Copyright Act (Article 25fa)", this publication was made available Green Open Access via the TU Delft Institutional Repository pursuant to Dutch Copyright Act (Article 25fa, the Taverne amendment). This provision does not affect copyright ownership.
Unless copyright is transferred by contract or statute, it remains with the copyright holder.

Sharing and reuse
Other than for strictly personal use, it is not permitted to download, forward or distribute the text or part of it, without the consent of the author(s) and/or copyright holder(s), unless the work is under an open content license such as Creative Commons.

Takedown policy
Please contact us and provide details if you believe this document breaches copyrights.
We will remove access to the work immediately and investigate your claim.

This work is downloaded from Delft University of Technology.

TU Delft

Delft University of Technology

Document Version
Final published version

Licence
CC BY

Citation (APA)
Hoogelander, M., Spirito, M., Sutbas, B., Carta, C., Llombart, N., & Alonso-delPino, M. (2026). Chessboard FPA in 130-nm SiGe BiCMOS for High-Resolution Passive Terahertz Imaging. *IEEE Journal of Microwaves*. https://doi.org/10.1109/JMW.2026.3660185

Important note
To cite this publication, please use the final published version (if applicable).
Please check the document version above.

Copyright
In case the licence states "Dutch Copyright Act (Article 25fa)", this publication was made available Green Open Access via the TU Delft Institutional Repository pursuant to Dutch Copyright Act (Article 25fa, the Taverne amendment). This provision does not affect copyright ownership.
Unless copyright is transferred by contract or statute, it remains with the copyright holder.

Sharing and reuse
Other than for strictly personal use, it is not permitted to download, forward or distribute the text or part of it, without the consent of the author(s) and/or copyright holder(s), unless the work is under an open content license such as Creative Commons.

Takedown policy
Please contact us and provide details if you believe this document breaches copyrights.
We will remove access to the work immediately and investigate your claim.

This work is downloaded from Delft University of Technology.

This article has been accepted for inclusion in a future issue of this journal. Content is final as presented, with the exception of pagination.

IEEE Journal of Microwaves

MTT-S MHz to THz Community

Received 20 November 2025; revised 26 January 2026; accepted 26 January 2026.

Digital Object Identifier 10.1109/JMW.2026.3660185

Chessboard FPA in 130-nm SiGe BiCMOS for High-Resolution Passive Terahertz Imaging

MARTIJN HOOGELANDER [1] (Student Member, IEEE), **MARCO SPIRITO** [1] (Member, IEEE), **BATUHAN SUTBAS** [2] (Member, IEEE), **CORRADO CARTA** [2] (Senior Member, IEEE), **NURIA LLOMBART** [1] (Fellow, IEEE), AND **MARIA ALONSO-DELPINO** [1] (Senior Member, IEEE)

(Regular Paper)

[1]Department of Microelectronics, Delft University of Technology, 2628CD Delft, The Netherlands
[2]Circuit-Design Department, IHP-Leibniz Institute for High Performance Microelectronics, 15236 Frankfurt – Oder, Germany

CORRESPONDING AUTHOR: Martijn Hoogelander (e-mail: m.hoogelander@tudelft.nl).

This work was supported by the National Growth Fund through the Dutch 6G Flagship Project “Future Network Services.”

ABSTRACT This work presents a chessboard focal plane array (FPA) camera with state-of-the-art thermal and spatial resolution in the 200–600 GHz frequency range. The FPA is implemented in a 130-nm SiGe BiCMOS technology, where each antenna element is loaded with a direct detector based on heterojunction bipolar transistors (HBTs). The antenna and detector architecture, including the vias and biasing network, were optimized to achieve a noise-equivalent power (NEP) suitable for passive THz imaging. Overall, the estimated loss of the FPA is better than 4 dB between 350 and 600 GHz, of which 1.5 dB is due to ohmic losses in the FPA, 1 dB to mutual coupling between detectors, and 0.7 dB to the impedance mismatch between the detector and antenna. A prototype of 24 pixels was manufactured and mounted on the base of a silicon hyperhemispherical lens with an anti-reflection coating. Excellent spatial resolution is achieved through a tight element spacing in the fabricated FPA, which is only half the wavelength in silicon at 350 GHz and therefore consistent with the state-of-the-art. Its responsivity, noise, and radiation patterns were characterized using a quasi-optical measurement setup. The measured radiation patterns are within 1 dB of simulations, demonstrating that the integrated THz camera achieves excellent spatial resolution. Between 330 GHz and 500 GHz, the NEP was measured to be on the order of 10 $\mathrm{pW}/\sqrt{\mathrm{Hz}}$. When considering the entire operational band, this NEP results in a noise-equivalent temperature difference (NETD) of the camera is 1.6 K for an integration time of 1 s per pixel, which is comparable to the state-of-the-art. While THz detectors with state-of-the-art sensitivity are limited to single-pixel designs, the presented work combines a multi-pixel implementation with competitive sensitivity.

INDEX TERMS Direct detectors, focal plane arrays, heterojunction bipolar transistors, integrated antennas, lens antennas, radiometers, terahertz imaging, thermal imaging, ultra wideband antennas.

I. INTRODUCTION

Direct detector designs integrated in commercial silicon platforms are increasingly capable of achieving the sensitivity required for passive THz imaging. CMOS-based designs operating at sub-THz frequencies, for example, have been demonstrated to achieve a noise-equivalent power (NEP) down to 10 $\mathrm{pW}/\sqrt{\mathrm{Hz}}$ [1], [2], [3]. Even beyond 1 THz, antenna-coupled direct detectors have been realized in various CMOS nodes, achieving an NEP on the order of 100 $\mathrm{pW}/\sqrt{\mathrm{Hz}}$ [4], [5], [6]. The NEP of designs using heterojunction bipolar transistors (HBTs) in SiGe BiCMOS technology is even lower, with the state-of-the-art achieving 7.9 $\mathrm{pW}/\sqrt{\mathrm{Hz}}$ [7] or even 2 $\mathrm{pW}/\sqrt{\mathrm{Hz}}$ [8]. When this performance can be maintained over hundreds of GHz of bandwidth, a noise-equivalent temperature difference (NETD) below 1 K can be realized [9], which has been considered sufficient for passive THz imaging [10].

To realize a THz camera suitable for imaging applications with a high spatial resolution and low NETD, sensitive direct detectors must be integrated into large, densely-sampled focal

© 2026 The Authors. This work is licensed under a Creative Commons Attribution 4.0 License. For more information, see https://creativecommons.org/licenses/by/4.0/

This article has been accepted for inclusion in a future issue of this journal. Content is final as presented, with the exception of pagination.

plane arrays (FPA) with an ultra-wide bandwidth. While large-scale focal plane array (FPA) imagers have been demonstrated at THz frequencies, either the device noise-equivalent power (NEP) was insufficient [11], or the antenna bandwidth was too limited [6], [12], [13] for passive imaging at the frequency of interest. Also in small-scale FPAs, the antenna bandwidth is often insufficient to achieve passive THz imaging, despite the use of state-of-the-art low-NEP detectors [3], [7]. Since these works utilize patch antennas, a low NEP is offset by a limited relative antenna bandwidth of at most 12.5 % [14], resulting in a high NETD. There are single-pixel or small-scale FPA imagers that use ring antennas [2], [8] or a biquad antenna [15] and combine a wideband atnenna with state-of-the-art detector NEP, therefore achieving (near-)passive NETD.

However, none of the aforementioned works feature antenna geometries that can simultaneously provide high radiation efficiency and the tight element spacing required for (near) diffraction-limited resolution. As explained in [16], [17], optimal spatial resolution is achieved when the antenna elements in the focal plane are spaced according to a diffraction-limited sampling of $d_\mathrm{f} = 0.5 f_\# \lambda$, with $f_\#$ being the F-number of the quasi-optical system and λ the wavelength. However, [16] also shows that such a tight element spacing traditionally comes at the cost of a spillover efficiency below 20 %, thus severely limiting the NETD of the imaging system. Consequently, the element size of state-of-the-art silicon-integrated THz imagers [2], [8], [15] only allows for sparsely sampled FPAs (i.e., $d_\mathrm{f} > f_\# \lambda$).

The highest focal plane sampling to date for these silicon integrated cameras at such high frequencies (i.e., $0.7 f_\# \lambda_\mathrm{Si} = 94\ \mu\mathrm{m}$ at 363 GHz) has been demonstrated by a chessboard FPA configuration integrated in 22-nm FD-SOI CMOS [18], [19]. The chessboard FPA consists of a connected array of tapered dipoles. This array geometry is self-complementary, enabling ultra wideband operation. Moreover, the polarization re-usage increases the focal plane sampling along the array diagonal with a factor of $\sqrt{2}$, resulting in the state-of-the-art spatial resolution of this FPA topology at only a 1-dB lower radiation efficiency compared to a state-of-the-art single-pixel design [20]. However, the CMOS-integrated chessboard FPA did not achieve passive imaging performance, as the NEP of the direct detectors was insufficient [18], [21].

This work presents the design of a chessboard FPA THz camera integrated in the SG13G2 technology, which is a 130-nm SiGe BiCMOS platform from IHP Microelectonics. Fig. 1 shows an overview of the proposed THz camera, which consists of a silicon lens with the FPA at its base. The operational bandwidth of the FPA is from 200 GHz to 600 GHz. The HBTs in this technology feature an $f_\mathrm{T}/f_\mathrm{max}$ of 350 GHz/450 GHz [22]. Compared to MOSFET-based detectors, HBT-based designs exhibit superior NEP due to their higher responsivity, particularly at higher operating frequencies [9]. Moreover, the input impedance of HBTs is less capacitive [23], thus intrinsically provide a better impedance match to the (chessboard) FPA antenna elements [24]. From the antenna point of view, the metal density requirements in the SiGe platform are significantly more relaxed compared to deeply-scaled CMOS nodes and therefore have a smaller impact on the antenna efficiency. Additionally, stronger leaky-wave propagation can be achieved in the SiO_2 cavity of the 130-nm SiGe technology, which features a 10.8-μm separation between the topmost metal and the substrate, compared to the 22-nm CMOS technology used in [18], where this separation was 8 μm. Although the enhanced leaky wave propagation is beneficial for the antenna directivity, it also increases the mutual coupling between surrounding elements and the associated losses. To reduce the mutual coupling, the element spacing in the chessboard FPA was increased from 92 μm to 108 μm along the diagonal.

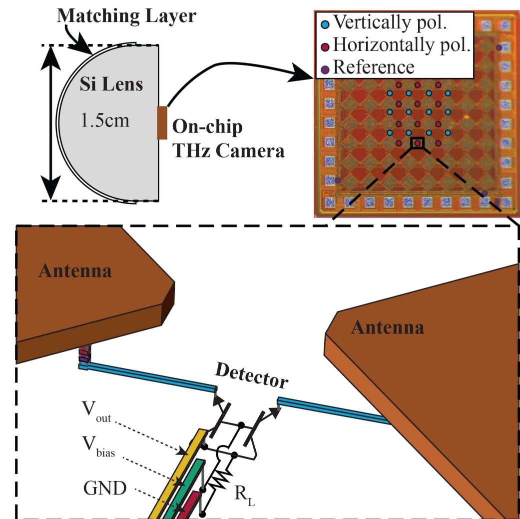

FIGURE 1. Overview of THz camera with an inset of the detector architecture.

By combining the qualities of HBT-based direct detectors and the chessboard FPA configuration, a THz camera can be realized with both an excellent NETD and spatial resolution. As the chessboard FPA configuration was already presented in [18], the emphasis of this work will be on the design of the detector architecture and adapting the chessboard FPA to the new back-end-of-line and the more dispersive and reactive detector impedance. To select the detector configuration, we compare the NEP and scalability of four single-stage transistor configurations. Detector designs with multiple transistor stages, such as pre-amplified detectors [25], [26] or cascodes [27], [28], are limited to operation up to approximately a third of $f_\mathrm{T}/f_\mathrm{max}$ and are therefore unsuitable for the sub-THz regime. Even below $f_\mathrm{T}/f_\mathrm{max}$, the integration of pre-amplification in an FPA is challenging. The pre-amplified, single-pixel detector reported in [25], for example, achieves excellent NEP, but demonstrates that every stage provides limited gain while requiring a silicon area on the order of 90 by 90 μm, which is considerable when compared to periodicity in the chessboard FPA. Moreover, the increased device count and metallization in the radiation path negatively impacts the antenna efficiency and radiation patterns.

The manuscript is structured as follows. In the next section, the performance of four different detector architectures

This article has been accepted for inclusion in a future issue of this journal. Content is final as presented, with the exception of pagination.

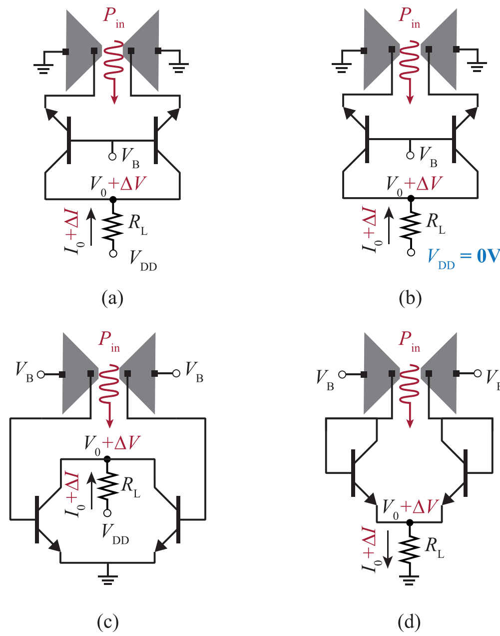

FIGURE 2. Four differential HBT-based detector topologies. (a) detector using CB stages in forward-active mode. (b) detector using CB stages in deep saturation. (c) detector using CE stages. (d) detector using diode-connected stages. The red signals indicate the terms corresponding to the input and output.

is compared to identify the detector best suited for integration into a dense FPA. In Section III, the chessboard FPA is translated to the SiGe platform and tuned to improve impedance matching with the detector. The fabricated chip, prototype assembly, and measurement setup are discussed in Section IV. Finally, the measurement results are presented in Section V.

II. DIRECT-DETECTOR TOPOLOGY IN 130-NM SIGE BICMOS

To select the optimum detector configuration in the SG13G2 technology, we review and compare the performance of the four transistor configurations shown in Fig. 2. The HBTs in the four topologies are configured, respectively, as common-base biased in forward-active mode (CB), common-base biased in deep saturation (CB–sat), common-emitter biased in forward-active mode (CE), and diode-connected. Detectors operating in the THz range based on the CB, CE and diode stages were compared in [29] in terms of current responsivity in a similar technology, but not in terms of the noise and input impedance. The performance of the CB stage, both in forward-active and in saturation, was thoroughly analyzed in [8], but not compared to the other two stages. In this section, we review all aforementioned configurations in terms of responsivity, output noise, impedance matching and scalability.

Literature shows that the CB and CE topologies achieve competitive performance well beyond 100 GHz. The CE detector, for instance, has been employed by [14] and [7], achieving an NEP of $21\,\mathrm{pW}/\sqrt{\mathrm{Hz}}$ and $7.9\,\mathrm{pW}/\sqrt{\mathrm{Hz}}$, respectively. The current state of the art is set by [8], [30], using CB and CB–sat detectors in the same 130-nm SiGe technology as this work. The diode-connected HBT configuration is not reported in literature, but is included for its compactness, and because its CMOS counterpart has been shown to achieve state-of-the-art NEP in [3]. An alternative detector based on the common-collector (CC) configuration is not explicitly considered, as its performance can be inferred from that of the CE and CB detectors. It will be discussed that a CC detector exhibits inferior performance to the aforementioned topologies.

Each of the four detector configurations consists of a differential pair of minimum-sized HBTs (i.e., using a single emitter with a length of 900 nm and width of 70 nm) and a resistor connected to the virtual ground to implement a voltage-mode readout. A differential design was chosen since it does not require additional passive components to decouple the RF from DC [31]. In such a configuration, the fundamental input frequency and its odd harmonics are shorted at the virtual ground located at the output. The DC response and (other) even harmonics, are not affected by the differential symmetry. Consequently, reading out the DC response from the output node is straightforward.

To compare the NETD of these detectors, simulations were performed using the HiCUM transistor model [32] in Keysight ADS. The NETD of the detector for an integration time τ_{int} can be determined from the detector NEP and the operational bandwidth according to [16]:

$$\mathrm{NETD} = \frac{1}{k_{\mathrm{B}}\sqrt{2\tau_{\mathrm{int}}}\int_{f_{\min}}^{f_{\max}}\frac{1}{\mathrm{NEP}}df}, \tag{1}$$

and where k_{B} is the Boltzmann constant, and $f_{\min}$ and $f_{\max}$ denote the lower and upper bounds of the operational band, respectively. The detector NEP, defined as the input-referred noise of the detector, is given by:

$$\mathrm{NEP} = \frac{v_{\mathrm{n,out}}^{\mathrm{tot}}}{\Re_{\mathrm{V}}}, \tag{2}$$

in which $\Re_{\mathrm{V}}$ is the (voltage) responsivity of the detector, defined by $\Re_{\mathrm{V}} = \Delta V/P_{\mathrm{in}}$, and $v_{\mathrm{n,out}}^{\mathrm{tot}}$ is the output noise of the detector. The following subsections discuss the different simulation types employed to study the parameters relevant to the detector NETD.

A. CURRENT AND VOLTAGE RESPONSIVITY

Especially when biased in forward-active mode, HBTs operate as a voltage-controlled current source. The low-frequency impedance between the collector and emitter is high, and the collector current is a strongly non-linear function of the base–emitter voltage. This non-linear relationship realizes the conversion of RF input power P_{in} to a DC (current) response ΔI, which is described by the detector current responsivity $\Re_{\mathrm{I}}^{\mathrm{det}} = \Delta I/P_{\mathrm{in}}$. Therefore, we first examine the intrinsic current responsivity of the HBTs in the four detector configurations.

Harmonic balance simulations were performed to find ΔI in response to the input power P_{in}. The input ports of the detectors were driven using a 50-Ω port and P_{in} was defined

This article has been accepted for inclusion in a future issue of this journal. Content is final as presented, with the exception of pagination.

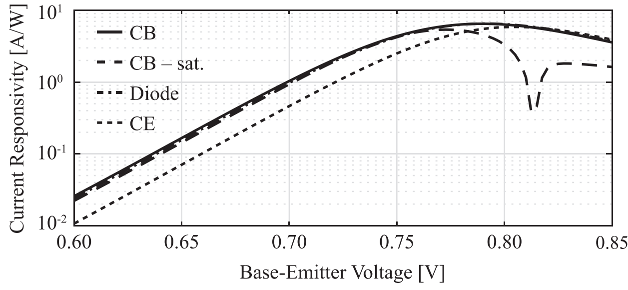

FIGURE 3. Current responsivity at 400 GHz as a function of V_{BE} for $R_L = 0\,\Omega$.

as the power accepted by the detector to find its intrinsic response. The influence of external loading was eliminated by setting the load resistor shown in Fig. 2 R_L to zero. The collector-emitter voltage V_{CE} of the CB and CE detectors was set to 1 V. In Fig. 3, the simulated $\Re_I^{det}$ is shown as a function of the base-emitter voltage V_{BE} at 400 GHz. Fig. 3 shows similar results for the CB, CB–sat and diode detectors, although the $\Re_I^{det}$ of the CB–sat detector rolls off at a lower V_{BE} and therefore has a slightly lower maximum. The CE detector performs significantly worse, as it operates beyond the given f_T. As was pointed out in [29], the CE stage outperforms the other detector configurations when used below f_T (i.e., 350 GHz).

Loading the HBT pair with the resistor transforms the current response ΔI into a voltage response ΔV. The resistance of the load provides a design parameter for the detector voltage responsivity $\Re_V^{det}$. When the HBT exhibits a high output impedance, $\Re_V^{det}$ scales linearly with R_L. However, this is not the case for all detector configurations and base-emitter voltages. As shown in Fig. 4(a), which depicts a simplified small-signal model of the CB detector, the current responses $\Re_I^{det} P_{in}/2$ of the two HBTs are subject to a current division between R_L and the output impedance of the detector pair $r_{out} = r_0/2$. This expression also holds for the other three configurations, for which the small-signal model is different only in direction of the response currents and/or the presence of the bias voltage source. The voltage responsivity $\Re_V^{det}$ is therefore given by:

$$\Re_V^{det} = \Re_I^{det} \frac{r_{out} R_L}{r_{out} + R_L}. \tag{3}$$

The low-frequency output impedance of the detector configurations is shown in Fig. 4(b). For the CB and CE detectors, where the HBTs operate in the forward-active region, r_{out} is very large. In this regime, the collector current I_C increases only slightly with the collector–emitter voltage V_{CE} due to the Early effect [33]. In contrast, r_{out} is orders of magnitude lower for the CB–sat and diode detectors, as I_C in these configurations depends much more strongly on V_{CE}. The impact of r_{out} on the voltage responsivity is illustrated in Fig. 4(c), which compares $\Re_V^{det}$ for the detector configurations at 400 GHz when loaded with a 10 kΩ resistor. The collector-emitter voltage V_{CE} of the CB and CE detectors was kept at a constant

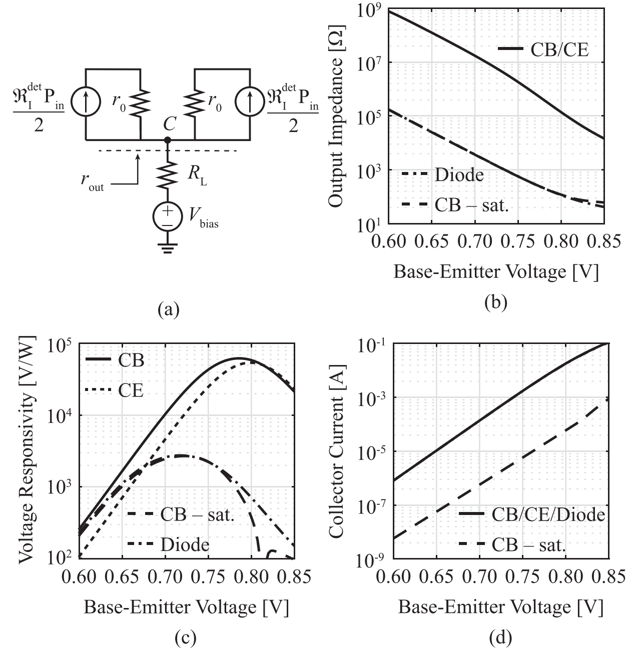

FIGURE 4. Impact of low-frequency output impedance r_{out} on detector voltage responsivity as a function of V_{BE}. (a) simplified small-signal model of CB detector near DC. The small-signal models of the CE, CB–sat and diode detectors is very similar. (b) low-frequency output impedance of parallel HBT pair. (c) Voltage responsivity at 400 GHz and R_L of 10 kΩ. (d) Collector current I_C.

level of of 1 V by increasing V_{bias} with the collector current I_C, to ensure transistor operation in forward-active mode.

Biasing the HBTs for maximum current responsivity, as shown in Fig. 3, yields an r_{out} only on the order of 100 Ω for the CB–sat and diode detectors. Consequently, $\Re_V^{det}$ is substantially lower for these configurations, and peaks at a smaller V_{BE} compared to the CB and CE detectors. Operating in deep saturation, however, does offer the advantage of minimal current consumption, as shown in Fig. 4(d).

The discussions above also clarify why a detector based on the common-collector (CC) configuration is undesirable. Similar to the CE detector, its current responsivity is limited by f_T, leading to reduced overall responsivity at higher frequencies. Furthermore, the CC stage exhibits a low output impedance, comparable to that of the diode detector [34]. A CC detector would therefore provide the lowest responsivity among the configurations considered.

B. OUTPUT NOISE AND NOISE-EQUIVALENT POWER

The detector responsivity and low-frequency output noise are equally important when aiming for passive performance. To study the noise performance of the detector configurations, the readout of the detectors was considered in the voltage domain (i.e., the voltage change ΔV across the load), and therefore the noise voltage at the output node was evaluated. Furthermore, it was assumed that the detector sensitivity is limited only by white noise contributions. This can be ensured by modulating the detector input signal at a frequency beyond the $1/f$-noise

IEEE Journal of Microwaves

MTT-S
MHz to THz Community

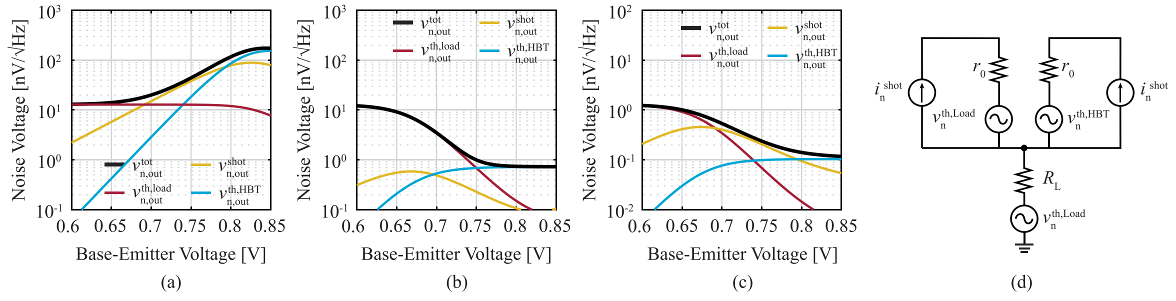

FIGURE 5. Output noise of the four detector topologies as a function of base-emitter voltage, with $R_L = 10\,\mathrm{k\Omega}$. (a) Noise voltage of CB and CE detectors. (b) Noise voltage of CB–sat detector. (c) Noise voltage of diode detector. (d) simplified small-signal model of the direct detector with the different noise contributions at low frequencies.

corner. The detector output noise is defined as $v_{\mathrm{n,out}}^{\mathrm{tot}}$, and is composed of the following contributions:

$$\left(v_{\mathrm{n,out}}^{\mathrm{tot}}\right)^2 = \left(v_{\mathrm{n,out}}^{\mathrm{shot}}\right)^2 + \left(v_{\mathrm{n,out}}^{\mathrm{th,HBT}}\right)^2 + \left(v_{\mathrm{n,out}}^{\mathrm{th,load}}\right)^2, \quad (4)$$

in which $v_{\mathrm{n,out}}^{\mathrm{shot}}$ is the noise voltage at the output node due to shot noise from the HBTs, $v_{\mathrm{n,out}}^{\mathrm{th,HBT}}$ due to thermal noise from the HBTs and $v_{\mathrm{n,out}}^{\mathrm{th,load}}$ due to thermal noise generated by the load. The individual contributions of $v_{\mathrm{n,out}}^{\mathrm{tot}}$ were determined using AC noise simulations in ADS, and are shown in Fig. 5(a)–(c) for the detector configurations of interest. Fig. 5(a) applies to both the CB and CE detectors, as they are identical in terms of noise.

The differences in noise performance between the configurations can be understood by inspecting the small-signal noise model shown in Fig. 5(d). It should be emphasized that the noise sources associated with the HBTs represent the combined effect of several underlying contributions. As explained in [35], [36], for example, the thermal noise consists of components from the base-spreading resistance and the contact resistances mapped to the output. The same applies to the shot noise originating from the collector current. According to [35], this contribution can be correlated either with the shot noise of the base–emitter current — when the device is biased in the forward-active region — or with the shot noise of the base–collector junction itself—when the device is biased in saturation.

Using the same approach as in [21], we can find the transfer of the noise sources in Fig. 5(d) to the output node, giving the following expressions for noise contributions in (4):

$$v_{\mathrm{n,out}}^{\mathrm{shot}} = i_{\mathrm{n}}^{\mathrm{shot}} \frac{r_{\mathrm{out}} R_{\mathrm{L}}}{r_{\mathrm{out}} + R_{\mathrm{L}}} = \sqrt{2qI_{\mathrm{C}}} \frac{r_{\mathrm{out}} R_{\mathrm{L}}}{r_{\mathrm{out}} + R_{\mathrm{L}}}, \quad (5)$$

$$v_{\mathrm{n,out}}^{\mathrm{th,HBT}} = v_{\mathrm{n}}^{\mathrm{th,HBT}} \frac{R_{\mathrm{L}}}{r_{\mathrm{out}} + R_{\mathrm{L}}}, \quad (6)$$

$$v_{\mathrm{n,out}}^{\mathrm{th,load}} = v_{\mathrm{n}}^{\mathrm{th,load}} \frac{r_{\mathrm{out}}}{r_{\mathrm{out}} + R_{\mathrm{L}}} = \sqrt{4k_{\mathrm{B}} T R_{\mathrm{L}}} \frac{r_{\mathrm{out}}}{r_{\mathrm{out}} + R_{\mathrm{L}}}, \quad (7)$$

where q is the elementary charge, T the temperature of the device, and k_{B} the Boltzmann constant.

For low V_{BE}, and for the CB and CE detectors in general, r_{out} is large and therefore the thermal noise from the

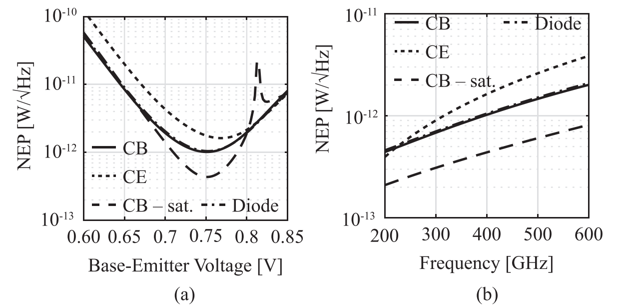

FIGURE 6. NEP of the four detector topologies with $R_L = 10\,\mathrm{k\Omega}$. (a) NEP at 400 GHz as a function of V_{BE}. (b) NEP at optimum V_{BE} versus frequency.

load dominates. As V_{BE} increases, the noise sources from the HBTs become dominant. For the CB and CE detectors, this is caused by the increasing collector current (and corresponding transistor gain), whereas for the diode and CB–sat detectors it is due to the changing balance between r_{out} and R_{L} in the voltage divisions. The CB–sat detector is minimally affected by shot noise, thanks to its low current consumption, as shown in Fig. 4(d).

The NEP, as defined in (2), is obtained by referring the output noise to the input of the detector. For the four detector topologies under consideration, it is shown in Fig. 6(a) at 400 GHz as a function of V_{BE} and in Fig. 6(b) as a function of frequency for the optimum V_{BE} at 400 GHz. Simulations show that the CB–sat detector, despite its lower responsivity, achieves the lowest NEP. This conclusion is consistent with [8], where the CB–sat and CB detectors were simulated and compared within the same technology.

C. OPTIMIZING THE LOAD RESISTOR FOR MINIMUM NEP

Both the voltage responsivity and noise contributions increase with R_{L}, according to (3) and (5)–(7). To investigate how this scaling translates to the NEP, the detector configurations were simulated with an R_{L} ranging from 10 Ω to 100 kΩ. The voltage responsivity, total output noise and NEP are shown in Fig. 7(a)–(c) as function of R_{L}, at a frequency of at 400 GHz and for a V_{BE} corresponding to the minimum NEP. The and the V_{BE} for optimum NEP is shown in Fig. 7(d).

This article has been accepted for inclusion in a future issue of this journal. Content is final as presented, with the exception of pagination.

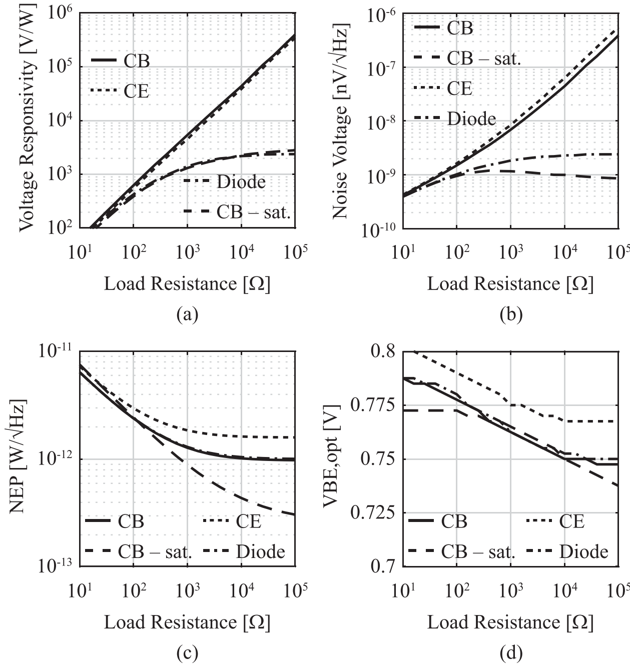

FIGURE 7. Detector performance at 400 GHz as a function of the load resistance R_L. (a) Voltage responsivity. (b) Output noise voltage. (c) Minimum NEP. (d) Bias voltage corresponding to minimum NEP.

For all detector configurations, it can be seen that the NEP stabilizes for large R_L. The minimum NEP can be found by first identifying the dominant noise contribution for each configuration, determining whether R_L or r_{out} is larger, and finally examining (5)–(7) for large R_L.

The CB, CE and diode detectors suffer mostly from shot noise near the optimum V_{BE} for NEP and/or responsivity. As R_L increases, the NEP can be approximated by dividing (5) by (3). Since the current divisions cancel out, the minimum NEP can be approximated by:

$$NEP_{\min}^{\text{CB/CE/diode}} \approx \frac{\sqrt{2qI_C}}{\Re_I^{\text{det}}}. \quad (8)$$

The output noise of the CB–sat detector, on the other hand, consists only of thermal noise. Like the other configurations, the thermal noise of the load dominates for small R_L or V_{BE} due to the voltage division between R_L and r_{out}. For larger R_L (or V_{BE}), the thermal noise contribution of the HBT starts dominating, and eventually the NEP can be approximated as follows:

$$NEP_{\min}^{\text{CB–sat}} \approx \frac{v_{\text{n,out}}^{\text{th,HBT}}}{\Re_I^{\text{det}} r_{\text{out}}}. \quad (9)$$

According to the foundry model, the term $v_{\text{n,out}}^{\text{th,HBT}}/r_{\text{out}}$ in (9) is significantly smaller than the shot noise $\sqrt{2qI_C}$ in the (8), hereby explaining the superior NEP of the CB–sat detector. Note that, in contrast to the CB detector, the thermal noise at the base and emitter terminals is not amplified to the output in the CB–sat detector.

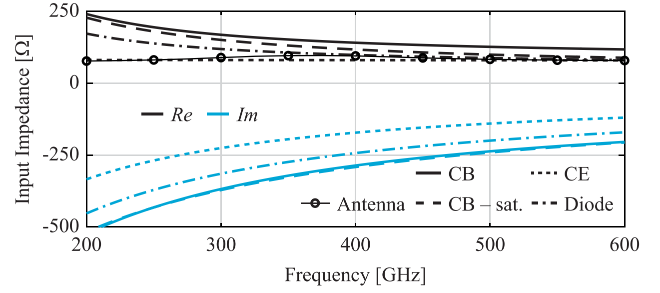

FIGURE 8. Detector impedance Z_{in} as a function of frequency of the different configurations at $V_{BE} = 0.75$ V.

Finally, Fig. 7(d) shows that the V_{BE} corresponding to the minimum NEP of the CB–sat and diode detectors decreases for larger R_L, which is a consequence of their relatively small r_{out}. From the current division in (3), choosing a large R_L causes the maximum responsivity to shift to lower V_{BE}, where r_{out} is larger. This also results in a slight decrease in the output noise of the CB–sat stage for larger R_L, as shown in Fig. 7(b). Since this configuration is dominated by $v_{\text{n,out}}^{\text{th,HBT}}$, (6) shows that a larger r_{out} reduces the transfer of $v_{\text{n}}^{\text{th,HBT}}$ to the output.

D. DETECTOR IMPEDANCE

Having discussed both responsivity and noise, the final characteristic influencing the NETD from the detector perspective is the input impedance. Fig. 8 shows the simulated input impedance of each detector configuration as a function of frequency at $V_{BE} = 0.75$ V. This bias condition is close to the optimum for all configurations in terms of NEP, as shown in Fig. 6(a). For reference, the antenna impedance R_{ant} of the chessboard FPA is also included in Fig. 8(a). Because the chessboard FPA is a self-complementary antenna embedded in the silicon stratification, its impedance at the feeding gaps is approximately 80 Ω (i.e., purely real) and remains nearly constant over a wide bandwidth.

Power transfer to the detector is maximized by ensuring that the antenna impedance is conjugately matched to the detector impedance. Evidently, all configurations suffer from a considerable input reactance and therefore require additional measures to improve the conjugate impedance match. Among them, the CE detector intrinsically provides the best match to the antenna impedance. Not only does it provide the least reactive input impedance, its input resistance is also very stable, and the closest to the antenna impedance.

To define an upper bound for the achievable conjugate matching, we assume that the reactive part of the detector can be perfectly compensated by the antenna, such that the chessboard FPA impedance becomes $Z_{\text{ant}}^{\text{ideal}} = R_{\text{ant}} - j\text{Im}\{Z_{\text{det}}\}$. Computing the conjugate reflection coefficient under this assumption shows that all configurations can potentially achieve a matching coefficient below −10 dB above 300 GHz, around the optimum V_{BE} of 0.75 V. The appealing impedance characteristics of the CE detector are therefore insufficient to compensate for its inferior NEP beyond f_T.

This article has been accepted for inclusion in a future issue of this journal. Content is final as presented, with the exception of pagination.

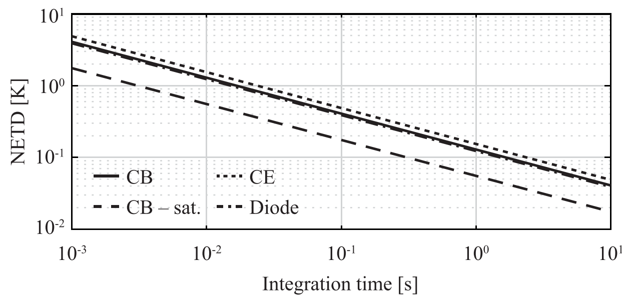

FIGURE 9. Intrinsic NETD of the detector configurations as a function of integration time, using a 10 kΩ load and biasing at the V_{BE} for minimum NEP.

The highly reactive and dispersive nature of the detector impedance complicates the realization of a good impedance match over the entire frequency range. Nevertheless, even without any impedance matching measures a moderate conjugate matching efficiency can be achieved. Using the results in Fig. 8 at 400 GHz as an example, the matching efficiency between the chessboard FPA impedance and the CE detector is 52 %, which represents the best case, whereas for the CB detector it is 43 %, representing the worst case. Section III discusses the losses arising from the absence of a conjugate impedance match in more detail, in particular for the CB–sat detector. From a system perspective, the higher mismatch at lower frequencies is partly mitigated by the higher responsivity in that region. It is not advisable to reduce matching losses by increasing the device size, as all current-related output noise increases proportionally with the device size. Furthermore, due to the smaller output impedance of larger HBTs, the responsivity decreases with increasing device size. As a result, any apparent improvement in impedance matching is offset by a degradation of the intrinsic detector performance.

E. INTRINSIC DETECTOR NETD

Ultimately, the detector configuration that provides the lowest NETD is preferred for implementation in the THz camera. Secondary considerations include characteristics that facilitate FPA scaling, such as detector current consumption and biasing complexity. Both aspects are evaluated and discussed in this section, followed by the selection of a configuration for implementation. To compare the detector configurations in terms of NETD, we use the simulated NEP of detectors with a 10-kΩ load, as depicted in Fig. 7. This value was chosen such that the best-case $1\,\mathrm{nV}/\sqrt{\mathrm{Hz}}$ noise floor of the instrumentation amplifier used for characterization [37], as discussed in Section V, does not exceed that of the CB–sat detector. The NETD is obtained by integrating the NEP according to (1) over the operational bandwidth ranging from 200 GHz to 600 GHz.

The result, shown in Fig. 9, confirms that the CB–sat detector should yield the best intrinsic NETD out of the considered configurations. The CE detector has the highest NETD, followed closely by the CB and diode detectors. Even though the CB detector does not achieve the lowest NETD, it is still an attractive option because of its high responsivity with respect to the CB–sat detector. This aspect makes the CB detector resilient to noise injected by external readout, as was also shown in [8]. For the same reason, the CE detector can be the preferred configuration when operating at lower frequencies [29], [38], [39], thanks to its high (current) responsivity below f_{T}.

It is straightforward to determine how much external noise can be accepted in the CB–sat detector before the CB detector becomes the preferred option. From (1), it follows that the NETD is proportional to $v_{\mathrm{n,out}}^{\mathrm{tot}}$. Any external noise will add to this incoherently. Given that the output noise of the CB–sat detector is $1\,\mathrm{nV}/\sqrt{\mathrm{Hz}}$ (Fig. 5), and that its NETD 2.3 times lower than that of the CB detector, it follows that the NETD of the CB–sat detector will exceed that of the CB detector when the readout injects an additional $2\,\mathrm{nV}/\sqrt{\mathrm{Hz}}$. Although this places a stringent constraint on the readout, instrumentation amplifiers with input-referred noise below this threshold are commercially available.

The CB–sat detector also provides advantages in terms of array scalability. Only a single supply is required for biasing, resulting in fewer metal lines in the array layout. Moreover, the supply does not need to be scaled to accommodate a high R_{L}. Due to this, and the fact that the CB–sat is biased in deep saturation, it consumes the least power out of the considered detector topologies. With the ultimate goal of realizing an FPA-based THz camera that is both passive and near diffraction-limited, the CB–sat was considered the best choice for implementation.

III. CHESSBOARD FPA DESIGN IN 130-NM SIGE BICMOS

In this section, the chessboard FPA design in 130-nm SiGe BiCMOS technology is presented. First, a general overview of the chessboard FPA implementation in this technology is given. Next, the impact of the reactive and dispersive detector impedance on mutual coupling and conjugate matching losses is examined, and the layout is adjusted around the feeding gaps to improve the impedance matching. Finally, the total losses and the resulting camera-level NEP are reported.

A. FPA GEOMETRY AND LAYER STACK

A close-up of the chessboard FPA geometry is shown in Fig. 10(a). The total array simulated in CST consisted of 7 × 8 antenna patches, corresponding to 7 × 7 vertically, and 8 × 6 horizontally polarized feeding points. This dimensioning ensures that the center point of the simulated structure coincides with the location of a (vertically polarized) feeding point. Only this central feeding point was excited using a discrete port; all other gaps were loaded using lumped elements with an impedance Z_{det}, representing the other detectors.

A periodicity of 152 μm was chosen as a trade-off between the mutual coupling between the elements and the beam overlap. Diagonally, the element separation is 108 μm, being $0.77 f_{\#}\lambda_{\mathrm{Si}}$ at 350 GHz. It should be noted that this periodicity is somewhat larger than the 92-μm (diagonal) element separation in the CMOS-integrated chessboard FPA [18],

This article has been accepted for inclusion in a future issue of this journal. Content is final as presented, with the exception of pagination.

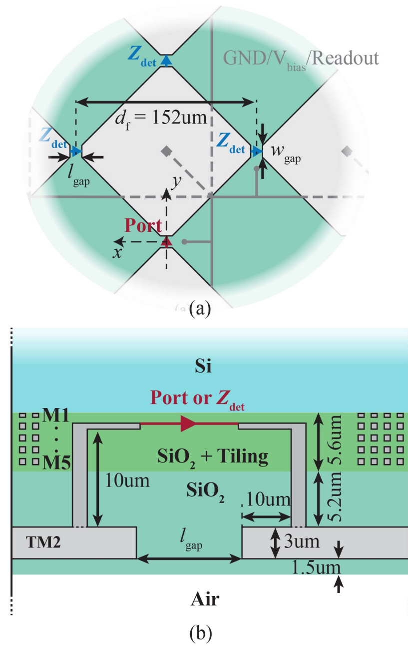

FIGURE 10. Geometry of chessboard FPA in 130-nm SiGe BiCMOS. (a) Close-up of simulated chessboard FPA geometry around the center. Only the central port was excited, all other ports were loaded with a lumped impedances Z_{det}. (b) Stratification of the chessboard FPA.

which is the result of the increased thickness of the SiO_2 cavity.

The stratification of the technology and the FPA is illustrated in Fig. 10(b). The technology contains two thick metal layers, TM1 and TM2, which have a thickness of 2 μm and 3 μm, respectively. The antenna was designed in the topmost metal layer of the technology (TM2) to minimize ohmic losses and to maximize the separation between the antenna and bulk silicon. The latter allows the propagation of a non-resonant leaky wave mode which is beneficial for the antenna directivity [40]. Additionally, there are five thin metal layers M1–M5, with thicknesses of 0.4 to 0.5 μm. As indicated in Fig. 10(b), the reference plane of the detector is defined at the M2 layer. The antenna geometry in Fig. 10(a) also shows the routing of the ground, biasing and readout lines, which are located in the lower five metal layers.

As with the CMOS array in [18], the FPA design must comply with the metal density rules of the technology. Therefore, square metal tiles of 1 μm in size were periodically distributed with a pitch 2 μm over the layout. Filling was only required in the layers M1–M5. No tiling was required in the thick metal layers, as their density requirements were fulfilled by the array and by using a high metal density in the pad ring. To include the effect of the tiling in simulations, the strategy from [40], [41] was employed to determine an equivalent anisotropic permittivity and permeability for the SiO_2 layers containing the thin metals. Because the metal density rules in the 130-nm SiGe technology are considerably more relaxed compared to the deeply scaled CMOS platform, the equivalent, relative permittivity of the cavity between the antenna and bulk silicon is lower in this work (i.e., $\varepsilon_r^{x,y,z} = 6.5$ and $\mu r^{x,y,z} = 0.9$) when compared to our previous designs [18], [40].

B. OPTIMIZING THE IMPEDANCE MATCH TO THE DETECTOR

A mismatched detector impedance influences two related loss mechanisms: the losses due to limited power transfer from the antenna to the detector, and the losses due to mutual coupling between array elements. The matching loss, L_{match}, is simply the matching efficiency η_{match} expressed in decibels. The mutual coupling loss, L_{MC}, is evaluated in CST by finding the total power absorbed by the lumped elements Z_{det}. This approach differs slightly from [18], where the mutual coupling loss in a chessboard FPA was evaluated only under matched feeding conditions. Since the CB–sat detector is clearly not well-matched to the chessboard FPA, a re-evaluation of the mutual coupling losses is required.

The FPA was simulated using different conditions of Z_{det} in the gap, although the gap of the central element was always excited using a 80-Ω port. Initially, all metals in the FPA were considered perfect electrical conductors, and the permittivity of the SiO_2 with metal tiling was approximated to be isotropic and equal to $\varepsilon_{\mathrm{r}} = 6$, and without the presence of the biasing and readout lines.

The input impedance and mutual coupling loss of the chessboard FPA under matched loading conditions are shown using the line with circular markers in Fig. 11. Both the lengths and widths of the gaps were 10 μm, the gaps were loaded directly in the antenna layer, and Z_{det} was set to 80 Ω. Fig. 11(a)–(b) show that the antenna input impedance under these loading conditions is very stable. Although no losses arise from the impedance matching, there are significant mutual coupling losses to the surrounding loads. Note that this scenario is practically identical to [18].

In reality, the FPA is loaded by the detector impedance $Z_{\mathrm{in}}^{\mathrm{CB-sat}}$ shown in Fig. 8(a). Simulating the FPA using $Z_{\mathrm{det}} = Z_{\mathrm{in}}^{\mathrm{CB-sat}}$ in the antenna layer yields the results indicated by the dotted lines in Fig. 11. Significant differences can be observed compared to the previous case, particularly at lower frequencies. Not only does the impedance mismatch reduce the power transfer to the detector, but it also decreases the power leakage to surrounding detectors. The observed ripples in the input impedance are attributed to reflections along the array due to the mismatched loads [42].

The impedance matching is significantly improved by an adequate sizing of the gaps, and by including the transitions from the antenna layer to the reference plane of the detector, located in M2. The dashed lines show the results obtained when these transitions are included, and the gap dimensions are 20 μm in length and 5 μm in width. The matching loss is approximately improved by 2 dB, and the mutual coupling losses are comparable to the previous case.

As a final step, we include metal and dielectric losses, the equivalent anisotropic SiO_2 layer with tiling, and the biasing, grounding, and readout lines. The lines were placed in

This article has been accepted for inclusion in a future issue of this journal. Content is final as presented, with the exception of pagination.

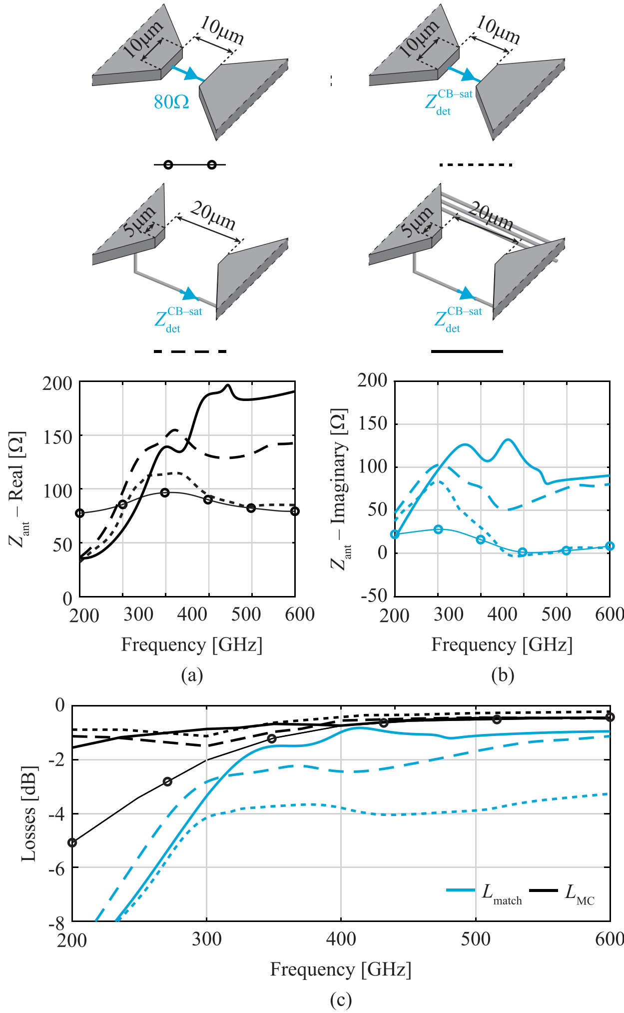

FIGURE 11. **Impedance matching between detector and chessboard FPA obtained from CST simulations using the illustrated conditions. (a) Real part of the input impedance Z_{ant} seen by the port. (b) Imaginary part of Z_{ant}. (c) Losses due to the impedance mismatch and mutual coupling.**

regions where they run minimally through regions of strong field intensity (i.e., around the gaps). Including these aspects in CST produces the results indicated by the solid lines in Fig. 11. It can be seen that the presence of the lines further increases the input resistance and reactance of the FPA, and slightly improves the impedance matching. Further tuning the location of the lines can result in a minor improvement of the matching below 300 GHz. However, the matching at the lower end of the band remains limited by the strongly dispersive nature of the detector impedance. The current line configuration provided the highest average matching across the band and therefore the lowest NETD.

C. CAMERA RESPONSIVITY

As was shown in Fig. 1, the THz camera consists of the chessboard FPA and a silicon lens. The losses of both components directly reduce the amount of power available to the detector, and therefore lower the responsivity on the camera

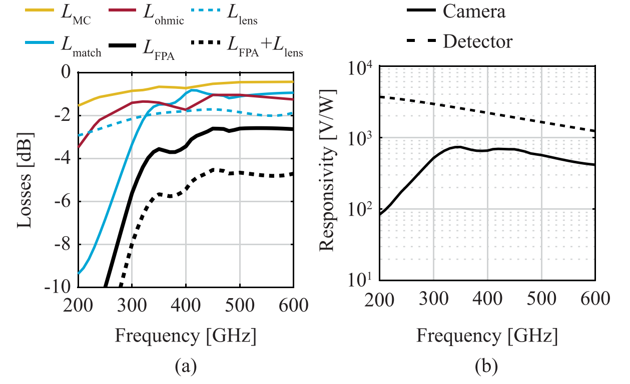

FIGURE 12. **Total impact of the chessboard FPA and silicon lens on the camera sensitivity. (a) Mutual coupling, matching and ohmic losses introduced by the chessboard FPA, and losses from silicon lens. (b) Detector-level responsivity and camara-level responsivity. Matching efficiency is included in the detector-level responsivity, but only considering the real part of the detector impedance.**

level. Therefore, the camera responsivity, $\Re_V^{cam}$, is defined as:

$$\Re_V^{cam} = \eta_{lens,Si}\eta_{FPA}\Re_V^{det}, \tag{10}$$

where η_{FPA} describes the losses from the integrated FPA and $\eta_{lens,Si}$ the losses from the silicon lens.

The loss term η_{FPA} was found from CST simulations. It comprises the mutual coupling loss, impedance matching loss, and ohmic loss from the metals and dielectrics (i.e., the bulk silicon and SiO_2 with metal tiling). The different contributions to the FPA losses are shown in Fig. 12(a). In total, the chessboard FPA introduces on the order of 4 dB of loss at 400 GHz. Compared to the CMOS-integrated chessboard FPA [18], the ohmic losses in the metal have risen from 0.5 dB to 1 dB, due to the reduced conductivity of the metal layers. In contrast, the ohmic losses in the dielectrics (including the metal tiling) remain unchanged. The most notable change is a pronounced increase in impedance matching losses at lower frequencies, caused by the dispersive nature of the detector impedance. This increase is partially offset by an improvement in the (related) mutual coupling losses.

The silicon lens is the same hyper-hemispherical lens as used in [43], of which the surface was coated with a parylene-C matching layer to reduce reflections at the silicon-air interface. The lens itself introduces spillover and reflection losses, which were computed using an in-house Fourier optics tool [44]. However, the lens loss is dominated by approximately 1.5-dB of ohmic loss arising from the parylene-C matching layer [45]. Although the matching layer does not improve the NEP (the additional ohmic losses negate the improvement in reflection losses) it does minimize the impact of reflections and standing waves in the quasi-optical system. An effective way of addressing the ohmic losses in the matching layer is by replacing the parylene-C coating with the lossless matching layer from [45], which is based on periodic, frusta-shaped features ablated into the lens surface. Fig. 12(a) shows the total loss introduced by the lens. The total radiation loss

This article has been accepted for inclusion in a future issue of this journal. Content is final as presented, with the exception of pagination.

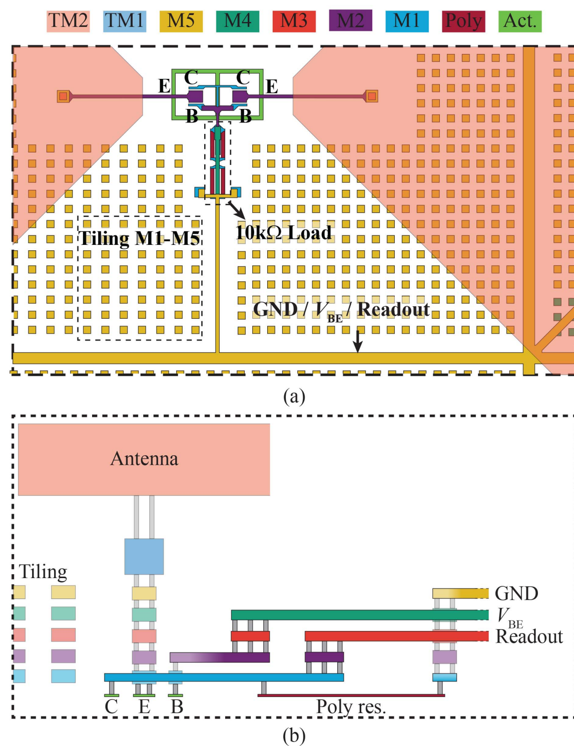

FIGURE 13. Layout around the feeding gap of the antenna. (a) Top-view. (b) Simplified side-view of the interconnect around the detector and load.

can be found from Fig. 12(a) to be 6.6 dB at 400 GHz, corresponding to a radiation efficiency (defined as $\eta_{\text{lens,Si}}\eta_{\text{FPA}}$) of 22 %.

The camera responsivity is shown in Fig. 12(b). For reference, the detector responsivity is also included. It can be seen that the impedance mismatch causes a significant deterioration in the voltage responsivity, especially at lower frequencies. Nevertheless, the camera responsivity is comparable to that of a single-pixel, state-of-the-art imager employing the same detector configuration [8]. Moreover, the chessboard FPA still achieves state-of-the-art spatial resolution [18], as the focal plane sampling is $0.77\lambda f_{\#}$ at 350 GHz, the frequency at which the camera responsivity reaches its maximum.

IV. PROTOTYPE ASSEMBLY AND CHARACTERIZATION

The chessboard FPA design presented in previous sections was implemented and taped out for characterization. A close-up of the layout around the feeding gap, detailing both the antenna and detector, is shown in Fig. 13. Several features are highlighted, such as the metal tiling, the 10 kΩ load resistor, and the HBTs. Also shown are the lines required for biasing, grounding and readout, all of which run parallel to each other in different metal layers to minimize the total, exposed area of these lines.

A close-up of the layout around an antenna feeding point is depicted in Fig. 13, and photographs of the fabricated chip are shown in Fig. 1 and Fig. 14(a). The FPA contains 112 integrated detectors, of which 8×7 belong to horizontally polarized pixels, and 7 × 8 belong to vertically polarized pixels. Although all detectors are operational, only the outputs of the 24 elements indicated in Fig. 1 were connected to bonding pads for readout. Four additional reference detectors (i.e., not connected to an FPA element) were placed around the FPA perimeter to minimize interconnect in the array itself. On-chip multiplexing would be required to provide access to all pixels and enable upscaling of the FPA, but is beyond the scope of this work. However, it could be realized using a column-parallel readout architecture based on bias-voltage control, as presented in [29].

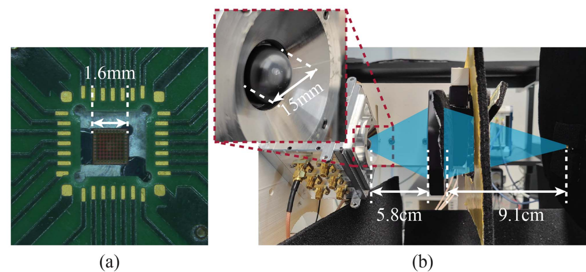

FIGURE 14. Assembly of the camera and measurement setup. (a) photograph of the chip (before bonding) inside the alignment pocket, and the PCB. (b) Photograph of the quasi-optical setup for characterization. The inset shows the silicon lens with a small damage on the matching layer.

The chip was glued to the base of the silicon, hyper-hemispherical lens from [43] and bonded to a PCB for biasing and readout. The lens, chip and PCB are all contained in an aluminum holder. Fabrication tolerances of the cavity in the aluminum holder (±50 μm) result in a worst-case lateral misalignment of 100 μm between the chip and the lens, which is comparable to the separation between adjacent elements along the diagonal. Pictures of the assembly (before bonding) and the relevant dimensions are shown in Fig. 14(a). The thickness of the chip substrate is 200 μm. As a result of the aspect ratio in the chip, the leakage losses from the chip are kept to a minimum.

V. MEASUREMENT RESULTS

The primary objective of the measurement campaign was to evaluate the NETD of the camera. Determining the NETD requires first characterizing the NEP, which in turn depends on the camera responsivity and output noise. To verify the spatial resolution, radiation patterns in the imaging plane were also measured.

The silicon lens and the quasi-optical (QO) setup from [43] were repurposed as a measurement setup to measure the radiation patterns and responsivity of the THz camera. Fig. 14(b) shows a photograph of the setup, with the camera assembly on the left-hand side. It should be noted that a small defect was observed in the parylene-C matching layer on the silicon lens, which may have affected the measurement results. In the center of the setup is a biconvex lens made of HDPE plastic, which refocuses the beams from the camera onto an imaging plane on the right-hand side. A standard-gain horn antenna,

This article has been accepted for inclusion in a future issue of this journal. Content is final as presented, with the exception of pagination.

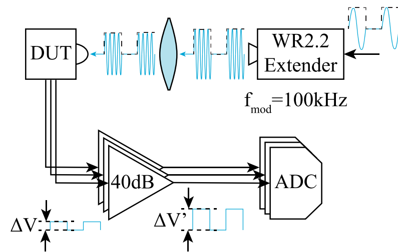

FIGURE 15. Measurement setup for characterizing the radiation patterns and responsivity in the spot.

aligned with the imaging plane, was used to illuminate the camera through the biconvex lens. To enable simultaneous characterization of both polarizations in the FPA, the camera was mounted at a 45° angle with respect to the horn, at the cost of an additional 3-dB polarization loss.

The horn antenna was driven by a WR2.2 frequency extender module from VDI. A schematic of the setup is shown in Fig. 15. The input signal to the extender module was ON–OFF modulated at 100 kHz to suppress the $1/f$ noise introduced by the integrated detector. The outputs of three detectors were amplified by individual INA849 low-noise instrumentation amplifiers (Texas Instruments) with a gain of 40 dB, corresponding to a bandwidth of 8 MHz [37], and subsequently digitized by three PXI-5122 analog-to-digital converters. The signal was integrated over 2.6 ms.

A. RADIATION PATTERNS

The measurements of the radiation patterns were conducted by moving the horn antenna planarly over the imaging plane using a CNC machine. The patterns are obtained by evaluating the corresponding voltage response of the camera, as the response is proportional to the power captured by the antenna.

The result of the pattern measurements in the spot are shown in Fig. 16. In Fig. 16(a), the 2D-pattern of all 24 pixels is shown at 400 GHz, normalized to their collective maximum. This result confirms the dense spacing of the beams and shows that all pixels are fully functional.

Fig. 16(b)–(d) respectively show the measured pattern of the central pixel along the E-, H- and two D-planes at the frequencies 350 GHz, 400 GHz and 500 GHz. Except in the D_2 plane, the main beams of the patterns at 350 GHz and 400 GHz have a good agreement with simulations. At 500 GHz, the match with simulations is worse.

The directivity of three measured pixels is shown in Fig. 16(e). The simulated directivity is also shown, both including and excluding the spillover losses from the silicon and plastic lenses. This provides a reasonable bound in which the measured directivity is expected. As can be seen, the measured value is within these two bounds up to 430 GHz. Above this frequency, the agreement with simulations decreases. Since this directivity degradation was not observed in our previous work [43] where we used the same QO setup, silicon lens, assembly procedure and a similar chessboard FPA [18], we believe that assembly tolerances are the most likely culprit. For example, a gap between the chip and the lens on the order of tens of microns can degrade the directivity by several decibels at these frequencies [46].

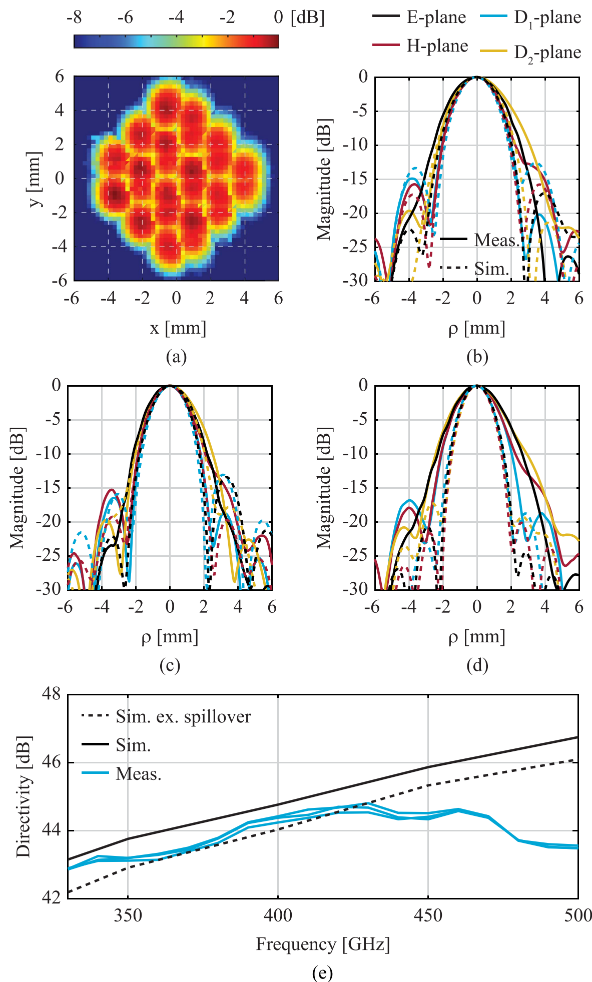

FIGURE 16. Measured radiation patterns in the imaging plane. (a) pattern measurement of all 24 pixels at 400 GHz. (b) Measured and simulated pattern of the central pixel at 350 GHz. (c) Measured and simulated pattern at 400 GHz. (d) Measured and simulated pattern at 500 GHz. (e) Measured and simulated directivity as a function of frequency. The directivity was measured for three pixels.

B. VOLTAGE RESPONSIVITY

Although the definition of the camera responsivity $\Re_V^{cam}$ in (10) does not account for losses introduced by the measurement setup, the measured voltage response is influenced by the choice of horn antenna and the biconvex lens. Consequently, the intrinsic camera responsivity $\Re_V^{cam}$ must be de-embedded from the overall coupling in the QO setup. Correcting for this coupling is conceptually equivalent to removing the path loss when characterizing a detector in the far-field, as was done in [8], [18], [21].

The losses introduced by the setup can be split into two parts: the efficiency of the biconvex lens, η_{BC}, and the field-matching efficiency η_{FM} between the pattern of the horn antenna and the patterns of the FPA. Using these terms, we

This article has been accepted for inclusion in a future issue of this journal. Content is final as presented, with the exception of pagination.

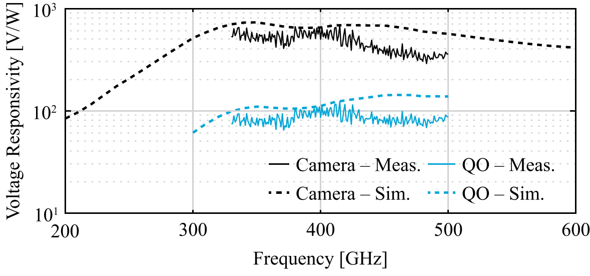

FIGURE 17. Measured and simulated voltage responsivity for a bias voltage of 0.75 V. Both the responsivity on the camera-level (i.e., excluding the losses of the biconvex lens and coupling to the horn) and the total responsivity are shown.

can define the quasi-optical responsivity $\Re_V^{QO}$ as follows:

$$\Re_V^{QO} = \eta_{FM}\eta_{BC}\Re_V^{cam}. \tag{11}$$

The terms η_{BC} and η_{FM} were simulated following the approach used in [43] to design this specific setup. First, the simulated patterns radiated by the silicon lens were propagated through the biconvex lens using TiCRA GRASP, from which the biconvex lens efficiency η_{BC} was determined. The biconvex lens introduces approximately 1 dB of total loss due to spillover, reflections, and ohmic loss. Secondly, the field matching efficiency η_{FM}, as defined in [43], was computed between the fields on the secondary side of the biconvex lens and the horn radiation pattern. The resulting η_{FM} was -8 dB at 330 GHz and -5.5 dB at 500 GHz. Note that these losses depend strongly on the horn antenna used in the spot and also include 3 dB of polarization loss.

The QO responsivity $\Re_V^{QO}$ can then be directly obtained from the measured voltage response using:

$$\Re_V^{QO} = \frac{\pi V_{out}^{LNA}(f_{mod})}{P_{CW}^{on} G_{LNA}}, \tag{12}$$

where $V_{out}^{LNA}(f_{mod})$ is the tone at the modulation frequency in the voltage spectrum at the LNA output, P_{CW}^{on} is the power radiated by the horn during continuous-wave operation, and G_{LNA} is the 40-dB gain of the LNA.

The camera responsivity $\Re_V^{cam}$ is obtained by equating (12) and (11). The measured and simulated camera and QO responsivities are shown in Fig. 17. Between 330 GHz and 430 GHz, the measured responsivity agrees with the simulated value within 1 dB. At higher frequencies, the deviation increases to between 2 dB and 2.5 dB, consistent with the decay observed in the directivity measurements. Nevertheless, the responsivity remains relatively stable across the WR2 band.

C. DETECTOR NOISE

The output noise of the detector was measured using the setup shown in Fig. 18. Except for the LNA, the setup is identical to that used in [21]. The camera, power supply, and LNA were all enclosed in a metal case to shield the system from ambient noise. The THz camera was biased using an AD5760 digital-to-analog converter (DAC), controlled remotely via an SPI interface. Two 12 V NiCd batteries served as a low-noise power source for both the LNA and the DAC. Noise characterization was performed using an SR785 dynamic signal analyzer (DSA), which has a bandwidth of 120 kHz. To suppress additional noise from the DSA, the gain of the INA849 LNA was increased to 55 dB. Although this higher gain reduces the LNA bandwidth, the overall measurement bandwidth is limited by the DSA rather than the LNA.

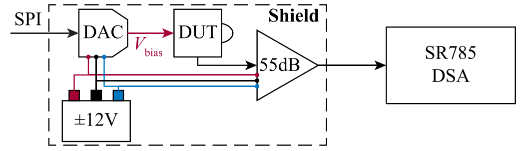

FIGURE 18. Setup used for noise characterization of the THz camera.

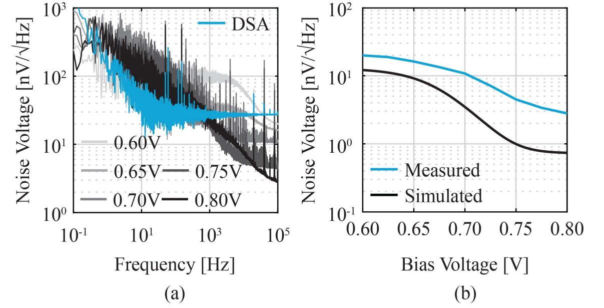

FIGURE 19. Measured detector and setup noise. (a) Measured output noise of the detector as a function of frequency, for various bias voltages. (b) Average measured and simulated detector noise as a function of bias voltage, in the bandwidth from 99 kHz to 120 kHz.

Before measuring the detector noise, the noise of the LNA and DSA was characterized. The noise floor of the DSA is around 10 nV/$\sqrt{\text{Hz}}$, which is suppressed to a negligible level by the LNA. The measured, input-referred noise floor of the LNA is slightly higher than expected [37]. Instead of 1.0 nV/$\sqrt{\text{Hz}}$, it was measured to be 1.7 nV/$\sqrt{\text{Hz}}$.

In order to acquire the standalone noise of the detector, the measured, input-referred noise of the LNA noise was non-coherently subtracted from the measured noise of the combination of the two. This was done using the relation:

$$\left(v_{n,out}^{tot}\right)^2 = \left(v_{n,out}^{meas}\right)^2 - \left(v_{n,in}^{LNA}\right)^2. \tag{13}$$

The different shades of gray in Fig. 19(a) show the measured detector noise $v_{n,out}^{tot}$ as a function of frequency for various bias voltages. The $1/f$ noise corner appears to be in the tens of kHz range for most bias voltages, but appears to shift beyond the bandwidth of the DSA at the highest bias levels. The $1/f$ noise corner is relatively high compared to the related design in [8], likely due to the small aspect ratio of the resistors [38], which were chosen for compactness relative to the antenna gap. Additionally, the measured spectra contain several spikes. Some of these spikes were already present in the measured noise spectrum of the DSA, which is also shown in Fig. 19(a) for reference. It is therefore suspected that these spikes originate from feedback or interference within the measurement setup.

This article has been accepted for inclusion in a future issue of this journal. Content is final as presented, with the exception of pagination.

TABLE 1. Comparison of Wideband, State-of-the-Art in THz Imagers Based on Antenna-Coupled Using Direct Detectors Integrated in Silicon Technology. Imagers With an LNA Between the Antenna and the Detector Are not Included. The NEP Bandwidth Is Defined as the Frequency Band in Which the NEP Is Below Twice its Minimum Value

Reference	Technology	Antenna	Element size at $\text{NEP}_{\min}$	$\text{NEP}_{\min}$ $[\text{pW}/\sqrt{\text{Hz}}]$	NEP Bandwidth [GHz]	NETD $\tau_{\text{int}} = 1\,\text{s}$ [K]
This work	**130 nm SiGe BiCMOS**	**$2 \times 3 \times 4$ chessboard**	**$0.5\lambda_{\text{Si}}$ at 350 GHz**	**7.5**	**250 – 600**	**1.6**[1]
[18]	22 nm FD-SOI CMOS	$2 \times 2 \times 3$ chessboard	$0.4\lambda_{\text{Si}}$ at 350 GHz	115	200 – 600[2]	14.7[3]
[8], [9]	130 nm SiGe BiCMOS	$1\times$ wire ring	$1.3\lambda_{\text{Si}}$ at 290 GHz	1.9	250 – 600	0.5
[2]	22 nm FD-SOI CMOS	3×3 wire ring	$1.0\lambda_{\text{Si}}$ at 855 GHz	12	700 – 1000[2]	2.0[3]
[3]	130 nm CMOS	8×8 patch	$0.5\lambda_0$ at 830 GHz	12.6	810 – 850	16.1[3]
[7]	130 nm SiGe BiCMOS	4×4 wire ring	$0.5\lambda_0$ at 250 GHz	7.9	230 – 280	8.1[3]
[47]	SBD in 130 nm CMOS	4×4 patch	$0.5\lambda_0$ at 250 GHz	29	270 – 290	74.3[3]
[14]	130 nm SiGe BiCMOS	4×4 patch	$0.5\lambda_0$ at 316 GHz	36	300 – 340	46.1[3]
[15]	65 nm CMOS	$1\times$ biquad	$1.5\lambda_{\text{Si}}$ at 1011 GHz	25	837 – 1290	2.8[3]

[1] Based on extrapolated NEP measurements in WR2 band.
[2] NEP bandwidth is not reported or shown, so the reported operational range of the antenna is shown here.
[3] Estimated under the assumption of a constant NEP across the (NEP) bandwidth, using the minimum reported NEP value.

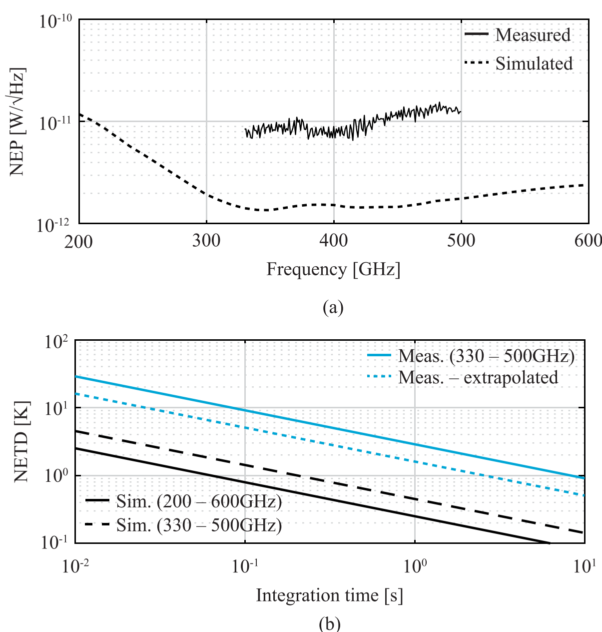

FIGURE 20. Measured and simulated sensitivity of the camera. (a) Measured and simulated NEP as a function of frequency at the optimum bias voltage of 0.75 V. (b) Measured and simulated NETD as a function of integration time. The two simulated values are obtained by integrating either over entire frequency range of interest, or only the WR2 band. The measured NETD is obtained by integrating over the WR2 band, and extrapolated to the entire band using the ratio between the two simulated results.

The average noise in a relatively quiet part of the spectra (i.e. from 99 kHz to 120 kHz) was chosen to find $v_{\text{n,out}}^{\text{tot}}$ as a function of bias voltage. The result is shown in Fig. 19(b) and compared to simulations. It can be seen that the measured noise is significantly higher than the value expected from simulations. At the optimum V_{BE} of 0.75 V, the noise was measured to be $4.5\,\text{nV}/\sqrt{\text{Hz}}$ instead of the expected $1.0\,\text{nV}/\sqrt{\text{Hz}}$. Since a device operating in deep saturation is not commonly used, it is reasonable to assume that the HBT models do not fully capture the (thermal) noise behavior in this regime [8]. Another possible explanation is that the DSA bandwidth is insufficient to observe the $1/f$ noise corner, meaning the results in Fig. 19(b) may still be flicker noise-limited. Despite the noise being higher than simulated, it is still comparable to that of a CB–sat detector implemented in the same technology [8]. Although the measured white noise of the 130-nm SiGe FPA is comparable to that of the detectors in the CMOS-integrated chessboard array [21], a substantial improvement in the $1/f$ noise is observed. The noise corner, previously estimated to lie in the low-MHz range for the 22-nm CMOS FPA, is on the order of 100 kHz for the FPA integrated in 130-nm SiGe.

D. ESTIMATION OF NETD FROM MEASUREMENT RESULTS

With both the voltage responsivity and the output noise characterized, the NEP and NETD of the THz camera can be computed. The measured and simulated NEP at the optimal bias voltage of 0.75 V are shown in Fig. 20(a). The measurements indicate that the realized THz camera achieves an NEP

This article has been accepted for inclusion in a future issue of this journal. Content is final as presented, with the exception of pagination.

of approximately $10\,\mathrm{pW}/\sqrt{\mathrm{Hz}}$, compared to the simulated value of around $2\,\mathrm{pW}/\sqrt{\mathrm{Hz}}$. This discrepancy is primarily due to the noise performance of the detector, and to a minor extent due to the lower responsivity.

The camera-level NETD is obtained by integrating the system-level NEP according to (1). Fig. 20(b) shows the measured and simulated NETD when integrating the NEP over different frequency bands. The solid black line represents the simulated camera NETD when integrating the NEP over the entire frequency range of interest (i.e., 200 GHz to 600 GHz). The camera, however, was only characterized in the WR2 band. To provide a fair benchmark, the NETD was also calculated based on the simulated NEP in only WR2 band, the result of which is shown by the dashed black line. The measured NETD is shown using the solid blue curve. The measured and simulated NETD, based on only the WR2 band, is 2.8 K and 0.44 K, respectively, for an integration time of 1 s per pixel. Note that the total integration time of the camera, to achieve the same NETD, increases when multiplexing between different pixels.

To estimate the realized NETD over the full frequency band of interest, it was assumed that the measured NETD in the WR2 band improves by the same factor as observed between the two simulated NETD values, indicated by the black lines. Applying this factor yields the dotted blue curve. Based on this extrapolation, the THz camera is estimated to achieve an NETD of 1.6 K for a 1-s integration time per pixel.

VI. CONCLUSION

A THz camera based on the chessboard FPA geometry with integrated direct detectors was designed and fabricated in the 130 nm SiGe BiCMOS technology from IHP Microelectronics. A detector based on deeply saturated HBTs in common-base configuration was used, as simulations showed this configuration had the lowest NEP and current consumption out of four considered detector topologies. The fabricated chessboard FPA features 24 accessible pixels with a pitch of $152\,\mu$m, yielding a near diffraction-limited focal plane sampling of $0.77\lambda_\mathrm{d} f_\#$ at 350 GHz, the frequency at which the responsivity is the highest.

The fabricated chessboard array was extensively characterized using a quasi optical measurement setup. Both the radiation patterns and responsivity showed an agreement within 1 dB of simulations. Above 450 GHz, a larger mismatch was observed, which can most likely be attributed to assembly tolerances. Noise measurements revealed that the output noise of the saturated common-base detector is significantly higher than expected, resulting in a higher NEP than predicted by simulations. Nevertheless, the achieved NETD of 1.6 K for a 1-s integration time per pixel should still enable near-passive and near-real-time imaging.

Table 1 compares the performance of the chessboard FPA in 130 nm SiGe BiCMOS with the state of the art. The table includes only wideband antenna-coupled direct detectors integrated in commercial silicon technologies. Since most works do not report the NETD, we estimated it using the NEP and the bandwidth in which the NEP remains below twice its minimum value. This bandwidth definition is also the one used in Table 1. The THz camera presented in this work achieves one of the lowest NEP values reported in literature. It also operates over a broader bandwidth than most comparable designs, which contributes to its low NETD. In addition, the focal-plane sampling — and thus the spatial resolution — of the chessboard FPA surpasses that of other FPAs. Overall, the proposed THz camera demonstrates competitive performance in terms of NEP, bandwidth, and especially spatial resolution.

ACKNOWLEDGMENT

We sincerely thank the IHP Leibniz Institut für Innovative Mikroelektronik for providing the access to the technology.

REFERENCES

[1] Z.-Y. Liu, F. Qi, Y.-L. Wang, P.-X. Liu, and W.-F. Li, "A multiband terahertz detector in 65-nm CMOS for spectroscopic imaging," *IEEE Trans. THz Sci. Technol.*, vol. 14, no. 6, pp. 781–790, Nov. 2024.

[2] R. Jain, R. Zatta, J. Grzyb, D. Harame, and U. R. Pfeiffer, "A terahertz direct detector in 22 nm FD-SOI CMOS," in *Proc. 13th Eur. Microw. Integr. Circuits Conf.*, 2018, pp. 25–28.

[3] D. Y. Kim, S. Park, R. Han, and K. O. Kenneth, "Design and demonstration of 820-GHz array using diode-connected NMOS transistors in 130-nm CMOS for active imaging," *IEEE Trans. THz Sci. Technol.*, vol. 6, no. 2, pp. 306–317, Mar. 2016.

[4] F. Ludwig, J. Holstein, A. Krysl, A. Lisauskas, and H. G. Roskos, "Modeling of antenna-coupled Si MOSFETs in the terahertz frequency range," *IEEE Trans. THz Sci. Technol.*, vol. 14, no. 3, pp. 414–423, May 2024.

[5] J. Holstein, R. Kapoor, J. A. Delgado Notario, V. Clericò, F. Ludwig, and H. G. Roskos, "Towards efficient and sensitive room-temperature THz detection using state-of-the-art broadband graphene/hBN-based TeraFETs," in *Proc. 49th Int. Conf. Infrared, Millimeter, THz Waves*, 2024, pp. 1–2.

[6] M. Liu et al., "A 3 THz CMOS image sensor," *IEEE J. Solid-State Circuits*, vol. 59, no. 9, pp. 2934–2947, Sep. 2024.

[7] K. Sengupta, D. Seo, L. Yang, and A. Hajimiri, "Silicon integrated 280 GHz imaging chipset with 4 × 4 SiGe receiver array and CMOS source," *IEEE Trans. THz Sci. Technol.*, vol. 5, no. 3, pp. 427–437, May 2015.

[8] M. Andree, J. Grzyb, R. Jain, B. Heinemann, and U. R. Pfeiffer, "Broadband modeling, analysis, and characterization of SiGe HBT terahertz direct detectors," *IEEE Trans. Microw. Theory Techn.*, vol. 70, no. 2, pp. 1314–1333, Feb. 2022.

[9] M. Andree, J. Grzyb, H. Rücker, and U. R. Pfeiffer, "Towards passive imaging with uncooled, low-NEP SiGe HBT terahertz direct detectors," *IEEE Trans. THz Sci. Technol.*, vol. 14, no. 5, pp. 632–651, Sep. 2024.

[10] C. Dietlein, A. Luukanen, F. Meyer, Z. Popovic, and E. Grossman, "Phenomenology of passive broadband terahertz images," in *Proc. ESA Workshop Millimetre-Wave Technol. Appl.*, Espoo, FI, USA, 2006, pp. 405–410.

[11] R. Al Hadi et al., "A 1 k-pixel video camera for 0.7–1.1 terahertz imaging applications in 65-nm CMOS," *IEEE J. Solid-State Circuits*, vol. 47, no. 12, pp. 2999–3012, Dec. 2012.

[12] S. Yokoyama et al., "5.8 A 32x32-Pixel 0.9 THz imager with pixel-parallel 12b VCO-Based ADC in 0.18 μm CMOS," in *Proc. IEEE Int. Solid-State Circuits Conf.*, 2019, pp. 108–110.

[13] M. Liu et al., "A 16.4kPixel 3.08-to-3.86 THz digital real-time CMOS image sensor with 73 dB dynamic range," in *Proc. IEEE Int. Solid-State Circuits Conf.*, 2023, pp. 4–6.

[14] M. Uzunkol, O. D. Gurbuz, F. Golcuk, and G. M. Rebeiz, "A 0.32 THz SiGe 4x4 imaging array using high-efficiency on-chip antennas," *IEEE J. Solid-State Circuits*, vol. 48, no. 9, pp. 2056–2066, Sep. 2013.

[15] M. Ferreras, D. Čibiraitė Lukenskienė, A. Lisauskas, J. Grajal, and V. Krozer, "Broadband sensing around 1 THz via a novel biquad-antenna-coupled Low-NEP detector in CMOS," *IEEE Trans. THz Sci. Technol.*, vol. 11, no. 1, pp. 16–27, Jan. 2021.

IEEE Journal of Microwaves
MTT-S MHz to THz Community

[16] S. van Berkel, O. Yurduseven, A. Freni, A. Neto, and N. Llombart, "THz imaging using uncooled wideband direct detection focal plane arrays," *IEEE Trans. THz Sci. Technol.*, vol. 7, no. 5, pp. 481–492, Sep. 2017.
[17] J. F. Johansson, "Millimeter-wave imaging theory and experiments," Onsala Space Observatory, Onsala, Sweden, Research Report, no. 151, 1986.
[18] M. Hoogelander et al., "Chessboard focal plane array for a CMOS-integrated terahertz camera," *IEEE Trans. THz Sci. Technol.*, vol. 13, no. 6, pp. 704–717, Nov. 2023.
[19] M. Hoogelander et al., "Diffraction-limited imaging demonstration using a silicon integrated array at terahertz frequencies," in *Proc. 47th Int. Conf. Infrared, Millimeter Terahertz Waves*, 2022, pp. 1–2.
[20] M. Andree, J. Grzyb, R. Jain, B. Heinemann, and U. R. Pfeiffer, "A broadband dual-polarized terahertz direct detector in a 0.13-μm SiGe HBT technology," in *Proc. IEEE MTT-S Int. Microw. Symp.*, 2019, pp. 500–503.
[21] S. v. Berkel et al., "Wideband modeling of CMOS schottky barrier diode detectors for THz radiometry," *IEEE Trans. THz Sci. Technol.*, vol. 11, no. 5, pp. 495–507, Sep. 2021.
[22] H. Rücker, B. Heinemann, and A. Fox, "Half-terahertz SiGe BiCMOS technology," in *Proc. IEEE 12th Topical Meeting Silicon Monolithic Integr. Circuits RF Syst.*, 2012, pp. 133–136.
[23] U. R. Pfeiffer, J. Grzyb, H. Sherry, A. Cathelin, and A. Kaiser, "Toward low-NEP room-temperature THz MOSFET direct detectors in CMOS technology," in *Proc. 38th Int. Conf. Infrared, Millimeter, THz Waves*, 2013, pp. 1–2.
[24] P. Hillger, J. Grzyb, R. Jain, and U. R. Pfeiffer, "Terahertz imaging and sensing applications with silicon-based technologies," *IEEE Trans. THz Sci. Technol.*, vol. 9, no. 1, pp. 1–19, Jan. 2019.
[25] J. Grzyb, M. Andree, H. Rücker, and U. Pfeiffer, "An on-chip antenna-coupled preamplified D-band to J-band total power radiometer chip in 130 nm SiGe BiCMOS technology," in *Proc. IEEE Radio Freq. Integr. Circuits Symp.*, 2024, pp. 359–362.
[26] R. B. Yishay and D. Elad, "Low Power 75–110 GHz SiGe Dicke Radiometer Front-End," in *Proc. IEEE MTT-S Int. Microw. Symp.*, 2021, pp. 885–887.
[27] B. Ustundag, E. Turkmen, B. Cetindogan, M. Kaynak, and Y. Gurbuz, "High responsivity power detectors for W/D-bands passive imaging systems in 0.1 μm SiGe BiCMOS technology," in *Proc. Asia-Pacific Microw. Conf.*, 2018, pp. 624–626.
[28] C. Herold, T. Mausolf, C. Carta, and A. Malignaggi, "A Broadband D-Band Power detector system in SiGe 130 nm BiCMOS technology," in *Proc. 18th Eur. Microw. Integr. Circuits Conf.*, 2023, pp. 145–148.
[29] R. Al Hadi, J. Grzyb, B. Heinemann, and U. R. Pfeiffer, "A terahertz detector array in a SiGe HBT technology," *IEEE J. Solid-State Circuits*, vol. 48, no. 9, pp. 2002–2010, Sep. 2013.
[30] J. Grzyb, M. Andree, R. Jain, B. Heinemann, and U. R. Pfeiffer, "A lens-coupled on-chip antenna for dual-polarization SiGe HBT THz direct detector," *IEEE Antennas Wireless Propag. Lett.*, vol. 18, no. 11, pp. 2404–2408, Nov. 2019.
[31] S. van Berkel, E. Malotaux, D. Cavallo, M. Spirito, A. Neto, and N. Llombart, "Wideband single pixel radiometer in CMOS," in *Proc. 42nd Int. Conf. Infrared, Millimeter, THz Waves*, 2017, pp. 1–2.
[32] M. Schröter and A. Chakravorty, *Compact Hierarchical Bipolar Transistor Modeling With HiCUM*. Singapore: World Scientific, 2010.
[33] D. Neamen, *Semiconductor Physics and Devices*, 4th ed. New York, NY, USA: McGraw Hill, 2012.
[34] B. Razavi, *Microelectronics*, 2nd ed. Hoboken, NJ, USA: Wiley, 2015.
[35] G. Niu, "Noise in SiGe HBT RF technology: Physics, modeling, and circuit implications," *Proc. IEEE*, vol. 93, no. 9, pp. 1583–1597, Sep. 2005.
[36] S. P. O. Bruce, L. K. J. Vandamme, and A. Rydberg, "Measurement of low-frequency base and collector current noise and coherence in SiGe heterojunction bipolar transistors using transimpedance amplifiers," *IEEE Trans. Electron Devices*, vol. 46, no. 5, pp. 993–1000, May 1999.
[37] T. Instruments, "INA849 ultra-low-noise (1 nV/$\sqrt{\text{Hz}}$), high-bandwidth, instrumentation amplifier datasheet," Texas Instruments, Dallas, Texas, Apr. 2021.
[38] S. Malotaux, M. Babaie, and M. Spirito, "A total-power radiometer front end in a 0.25- μm BiCMOS technology with low $1/f$ -corner," *IEEE J. Solid-State Circuits*, vol. 52, no. 9, pp. 2256–2266, Sep. 2017.
[39] J. W. May and G. M. Rebeiz, "Design and characterization of W-Band SiGe RFICs for passive millimeter-wave imaging," *IEEE Trans. Microw. Theory Techn.*, vol. 58, no. 5, pp. 1420–1430, May 2010.
[40] S. van Berkel et al., "Wideband double leaky slot lens antennas in CMOS technology at submillimeter wavelengths," *IEEE Trans. THz Sci. Technol.*, vol. 10, no. 5, pp. 540–553, Sep. 2020.
[41] D. Cohen and R. Shavit, "Bi-anisotropic metamaterials effective constitutive parameters extraction using oblique incidence S-parameters method," *IEEE Trans. Antennas Propag.*, vol. 63, no. 5, pp. 2071–2078, May 2015.
[42] D. Cavallo and A. Neto, "A connected array of slots supporting broadband leaky waves," *IEEE Trans. Antennas Propag.*, vol. 61, no. 4, pp. 1986–1994, Apr. 2013.
[43] M. Hoogelander, R. van Dijk, M. Spirito, N. Llombart, and M. Alonso-delPino, "Demonstration of near diffraction-limited terahertz images using a CMOS-Integrated chessboard array," *IEEE Trans. THz Sci. Technol.*, vol. 14, no. 4, pp. 531–536, Jul. 2024.
[44] H. Zhang, S. O. Dabironezare, G. Carluccio, A. Neto, and N. Llombart, "A fourier optics tool to derive the plane wave spectrum of quasi-optical systems [EM programmer's notebook]," *IEEE Antennas Propag. Mag.*, vol. 63, no. 1, pp. 103–116, Feb. 2021.
[45] J. Bueno, S. Bosma, T. Bußkamp-Alda, M. Alonso-delPino, and N. Llombart, "Lossless matching layer for silicon lens arrays at 500 GHz using laser ablated structures," *IEEE Trans. THz Sci. Technol.*, vol. 12, no. 6, pp. 667–672, Nov. 2022.
[46] M. Alonso-delPino, S. Bosma, C. Jung-Kubiak, J. Bueno, G. Chattopadhyay, and N. Llombart, "A transmit lens array with high-gain and beam-steering capabilities at submillimeter wavelengths," *IEEE Trans. THz Sci. Technol.*, vol. 14, no. 1, pp. 64–75, Jan. 2024.
[47] R. Han et al., "Active terahertz imaging using Schottky diodes in CMOS: Array and 860-GHz pixel," *IEEE J. Solid-State Circuits*, vol. 48, no. 10, pp. 2296–2308, Oct. 2013.

MARTIJN HOOGELANDER (Student Member, IEEE) received the B.Sc. (cum laude) and M.Sc. degrees in electrical engineering in 2017 and 2021, respectively, from the Delft University of Technology (TU Delft), Delft, The Netherlands, where he is currently working toward the Ph.D. degree with Terahertz Sensing Group. During his master's degree, he specialized in microelectronics, with an emphasis on RF/wireless design with Electronics Research Laboratory, TU Delft. His research interests include passive imaging at submillimeter wavelengths and integrated circuits for antenna-coupled direct detectors.

MARCO SPIRITO (Member, IEEE) received the M.Sc. degree (cum laude) in electrical engineering from the University of Naples Federico II, Naples, Italy, in 2000, and the Ph.D. degree in microelectronics from the Delft University of Technology, Delft, The Netherlands, in 2006. From 2000 to 2001, he was a Guest Researcher with Infineon Technologies, Munich, Germany. In 2006, he joined the Department of Electronics and Telecommunications Engineering, University of Naples Federico II. In 2008, he joined as an Assistant Professor with Electronics Research Laboratory, Delft University of Technology, where he has been an Associate Professor since 2013. In 2010 and 2017, he was one of the Co-Founder of Anteverta-MW, Eindhoven, The Netherlands, and Vertigo Technologies, Delft, respectively, two companies pioneering innovative measurement techniques and instruments. His research interests include the development of advanced passive components and building blocks operating in the millimeter and submillimeter frequency ranges, development of characterization setups and calibration techniques for millimeter and submillimeter waves, and design and integration of millimeter-wave sensing systems. Dr. Spirito was the recipient of the Best Student Paper Award for his contribution to the 2002 IEEE Bipolar/BiCMOS Circuits and Technology Meeting and IEEE Microwave Theory and Techniques Society Microwave Prize in 2008. He was the co-recipient of the Best Student Paper Award at the 2011 IEEE Radio Frequency Integrated Circuits Symposium, GAAS Association Student Fellowship in 2012, the Best Student Paper Award in second place at the 2018 International Microwave Biomedical Conference, the Best Paper Award at the 2019 Winter ARFTG Conference, and the Best Student Paper Award at the 2019 Summer ARFTG Conference.

This article has been accepted for inclusion in a future issue of this journal. Content is final as presented, with the exception of pagination.

BATUHAN SUTBAS (Member, IEEE) received the B.Sc. and M.Sc. degrees in electrical and electronics engineering from Bilkent University, Ankara, Türkiye, in 2016 and 2019, respectively, and the Ph.D. (summa cum laude) degree in electrical engineering from the Brandenburg University of Technology, Cottbus, Germany, in 2024. From 2016 to 2019, he was a MMIC Design Engineer with Nanotechnology Research Center, Bilkent University, and ABMicroNano Inc., Ankara, where he was involved in the design and development of GaN-based PAs. Since 2019, he has been a Scientist with Circuit-Design Department, IHP–Leibniz Institute for High Performance Microelectronics, Frankfurt (Oder), Germany, where he has been leading the Millimeter-Wave and THz Sensor Circuits Team, since 2023. His research interests include mm-Wave and sub-THz systems, and circuits particularly for sensing applications.

CORRADO CARTA (Senior Member, IEEE) was born in Cagliari, Italy. He received the master's degree in electrical engineering from the University of Cagliari, Cagliari, in 2000, and the Ph.D. degree from the Swiss Federal Institute of Technology (ETH) Zürich, Zürich, Switzerland, in 2006. From 2000 to 2006, he was with Microwave Electronics Group, ETH Zürich, where his research interests included silicon radio frequency integrated circuit design for microwave wireless communications. From 2006 to 2008, he was with High-Speed Electronics Group, Department of Electrical and Computer Engineering, University of California at Santa Barbara, Santa Barbara, CA, USA, where his research work focused on the design of silicon integrated circuits for very large millimeter-wave phased arrays. In 2008, he joined Sonos Inc., Santa Barbara, where he led the RF Engineering and Compliance Team, involved in the development and characterization of the wireless interface of new and existing products. In 2010, he joined the Chair of Circuit Design and Network Theory, Technische Universität Dresden, Dresden, Germany, where he led the mm-Wave IC Design Group and the Beyond Moore Electronics Group. Since 2022, he has been a Professor with Technische Universität Berlin and Chair of Broadband and High-Frequency Integrated Circuits, with a joint appointment as the Head of the Circuit-Design Department, Leibniz Institute for High Performance Microelectronics, Frankfurt (Oder), Germany, conducting research on a wide range of topics, including integrated microwave and millimeter-wave circuits, broadband mixed-signal circuits, high-efficiency circuits for communication and sensor applications.

NURIA LLOMBART (Fellow, IEEE) received the master's degree in electrical engineering and the Ph.D. degree from the Polytechnic University of Valencia, Valencia, Spain, in 2002 and 2006, respectively. During her master's degree studies, she spent one year with the Friedrich Alexander University of Erlangen Nuremberg, Erlangen, Germany, and was with the Fraunhofer Institute for Integrated Circuits, Erlangen. From 2002 to 2007, she was with Antenna Group, TNO Defense, Security and Safety Institute, The Hague, The Netherlands, as a Ph.D. Student and Researcher. From 2007 to 2010, she was a Postdoctoral Fellow with the California Institute of Technology, Submillimeter Wave Advance Technology Group, Jet Propulsion Laboratory, Pasadena, CA, USA. She was a "Ramón y Cajal" Fellow with Optics Department, Complutense University of Madrid, Madrid, Spain, from 2010 to 2012. In 2012, she joined the THz Sensing Group, Technical University of Delft, Delft, The Netherlands, where she has been a Full Professor since 2018. She has coauthored more than 200 journal and international conference contributions in the areas of antennas and THz systems. Dr. Llombart was the co-recipient H. A. Wheeler Award for the Best Applications Paper of 2008 in the IEEE Transactions on Antennas and Propagation, 2014 THz Science and Technology Best Paper Award of the IEEE Microwave Theory and Techniques Society, and several NASA awards. She was also the recipient of the 2014 IEEE Antenna and Propagation Society Lot Shafai Mid-Career Distinguished Achievement Award. She is a Board Member of the IRMMW-THz International Society and Associate Editor for IEEE TRANSACTION ON ANTENNAS AND PROPAGATION. In 2015, she was the recipient of European Research Council Starting Grant. In 2019, she became IEEE fellow for contributions to millimeter and submillimeter wave quasi-optical antennas.

MARIA ALONSO-DELPINO (Senior Member, IEEE) received the degree in telecommunications engineering from the Technical University of Catalonia (UPC), Barcelona, Spain, in 2008, the M.S. degree in electrical engineering from the Illinois Institute of Technology, Chicago, IL, USA, in 2008, and the Ph.D. degree in signal theory and communications/electrical engineering from UPC in 2013. From 2014 to 2015, she was a Postdoctoral Researcher with the Technical University of Delft (TU Delft), Delft, The Netherlands. From 2015 to 2016, she was a NASA Postdoctoral Fellow with Jet Propulsion Laboratory (JPL), Pasadena, CA, USA. From 2016 to 2020, she was a Member of the Technical Staff with Sub-millimeter Wave Advanced Technology Group, JPL/NASA. Since 2020, she has been an Assistant Professor with TU Delft. Her research interests include millimeter and submillimeter-wave heterodyne and direct detection receiver technologies, antennas, and quasi-optical systems. Dr. Alonso-Delpino was the recipient of the Outstanding Reviewer Award of the IEEE TRANSACTIONS ON TERAHERTZ SCIENCE AND TECHNOLOGY in 2013 and co-recipient of the 2014 IEEE Terahertz Science and Technology Best Paper award, and the 2022 European Conference on Antennas and Propagation Best Antenna Design Paper award.